

# Acceptance and resolution simulation studies for the dielectron spectrometer HADES at GSI

R. Schicker<sup>a,1</sup>, A. Brenschede<sup>b</sup>, K. Garrow<sup>c,2</sup>, H. Schon<sup>c</sup>,  
A. Balanda<sup>d</sup>, H. Bokemeyer<sup>c</sup>, J. Friese<sup>e</sup>, W. Karig<sup>f</sup>, P. Kienle<sup>e</sup>,  
W. Koenig<sup>c</sup>, W. Kuhn<sup>b</sup>, F. Lefevre<sup>c,3</sup>, V. Metzger<sup>c,b</sup>, G. Roche<sup>g</sup>,  
P. Salabura<sup>d</sup>, A. Schroter<sup>c,4</sup>, J. Stroth<sup>f</sup> and H. Tsertos<sup>a</sup>

<sup>a</sup>University of Cyprus, Nicosia, Cyprus

<sup>b</sup>University G iessen, Germany

<sup>c</sup>GSI Darmstadt, Germany

<sup>d</sup>Jagellonian University Cracow, Poland

<sup>e</sup>TUM Munich, Germany

<sup>f</sup>University Frankfurt, Germany

<sup>g</sup>University of Clermont-Ferrand, France

---

## Abstract

Design studies for a second generation Dielectron Spectrometer to be built at the SIS accelerator of GSI Darmstadt are presented. The basic design parameters of this system are specified and the different detector components for charged particle tracking and for lepton identification are described. The geometrical acceptance for lepton pairs is given. Results on single track momentum resolution and on lepton pair mass resolution are reported.

---

<sup>1</sup> Corresponding author, e-mail "schicker@alpha2.nsc.ucy.ac.cy"

Dept. Nat. Science, Univ. Cyprus, P.O. 537, 1678 Nicosia, Cyprus

<sup>2</sup> Now at University of Saskatchewan, Canada

<sup>3</sup> Now at Ecole des Mines, Nantes, France

<sup>4</sup> Now at Blaupunkt, Germany

## 1 Introduction

Dileptons emitted in relativistic nucleus-nucleus collisions are of great interest because once produced, they are not subject to strong final state interactions with the surrounding nuclear medium. Thus, they carry information from the inside of strongly interacting matter to the outside world, and bring forth information not accessible by measuring purely hadronic final states. Dileptons are therefore the ideal probe to study the behavior of nuclear matter under extreme conditions produced in relativistic heavy-ion collisions. The dynamics of heavy-ion reactions at relativistic energies is dominated by cascades of elementary hadron reactions. At the SIS energies of 1-2 A GeV, a substantial fraction of the participating nucleons is excited to baryonic resonances which subsequently decay predominantly by pion emission. The measurement of radiative decays of the baryonic resonances offers a new perspective for investigating the behavior of this resonance matter. However, a quantitative understanding of nuclear resonance matter necessitates detailed knowledge of elementary cross sections and of hadron structure. Form factors describing the electromagnetic structure of hadrons are presently largely unknown, but are accessible in the space-like region by electron scattering experiments and in the time-like region by measuring radiative decays of meson and baryon resonances. These resonances can be selectively produced with high production cross section in pion induced reactions. Thus, a comprehensive program in relativistic heavy-ion physics has to rely on a vigorous pion program providing information on elementary hadron physics. Furthermore, improved knowledge of hadron structure is of great interest as it is pertinent for a better understanding of the nonperturbative regime of Quantum Chromodynamics (QCD), the theory of strong interactions. In relativistic nuclear physics, pioneering dilepton spectroscopy work has been done by the DLS collaboration [1,2] at the BEVALAC and by the CERES collaboration [3,4] at the CERN SPS. The ongoing interest in this field has led to a number of topical workshops and culminated in the proposition of the second generation High Acceptance Dielectron Spectrometer HADES [5,6]. This spectrometer will be installed at the heavy-ion synchrotron SIS at GSI Darmstadt. A new, dedicated beam line will deliver light and heavy-ion beams in the energy range of 1-2 A GeV. Moreover, the great interest in improved data from pion induced reactions led to the elaboration of a secondary pion beam facility at SIS. This facility will provide HADES with pion beams of momenta between 0.5 GeV/c and 2.5 GeV/c [7]. The purpose of this paper is to present design studies for the HADES spectrometer and to outline some of its performance characteristics. This paper is organized as follows: Section 2 gives a summary on the different sources of interest in dilepton spectroscopy of dense nuclear matter. In section 3, the design principles of the spectrometer are explained. Then, in section 4, the chosen field configuration is described. Section 5 introduces the HADES spectrometer including the different detector components for tracking and for lepton identification. The

spectrometer acceptance is presented in section 6 together with the anticipated resolution performance as obtained in a GEANT simulation.

## 2 Dilepton sources

### 2.1 Vector mesons $\rho$ , $\omega$ , $\phi$

In the study of hot and dense matter, dielectron decays of the vector mesons  $\rho$ ,  $\omega$  and  $\phi$  are of particular interest. Due to its short lifetime, the  $\rho$  meson decays with high probability during the high density phase. On the contrary, the  $\omega$  and  $\phi$  mesons decay mostly outside of the high density region. However, the probability for decay within the high density region does not only depend on intrinsic lifetime but also on momentum. The probability for decay within the dense phase can be increased or reduced by selecting mesons with low and high momenta, respectively. The behavior of these vector mesons is of particular interest since chiral symmetry is expected to be partially restored in dense nuclear matter. Chiral symmetry restoration is evidenced in a decrease of the magnitude of the chiral condensate with a corresponding decrease of the constituent quark mass. In-medium vector meson masses are thus modified, reflecting the change in constituent quark mass. The in-medium vector meson mass is a measurable quantity through the kinematic reconstruction of the lepton pair. Thus, one can verify experimentally whether the in-medium vector meson mass deviates from its vacuum value by examining in-medium decays. Based on effective chiral Lagrangians with incorporation of QCD scaling, a 20% reduction of the  $\rho$  mass at normal ground state density has been deduced [8]. Model calculations predict the chiral condensate to depend on nuclear density [9]. Hence, pion induced vector meson production tests the chiral condensate at almost ground state density, whereas heavy-ion induced reactions do so at different values up to three times ground state density. QCD sum rules also predict a change of vector meson masses in the nuclear medium [10]. Whereas a large mass shift is predicted for the  $\rho$  meson at twice ground state density, the  $\omega$  mass is thought to shift less due to the small strangeness content of the nucleon [11]. A mass shift of the  $\rho$  meson affects the in-medium decay branching ratios into the dilepton and kaon channels. Hence, the in-medium behavior of the kaons is additionally of great interest [12]. The behavior of vector mesons in dense matter, in particular the  $\rho$  meson, has also been studied within the framework of hadronic models. These studies predict a broadening of the peak of the  $\rho$  meson spectral function without an appreciable shift of the centroid [13,14]. The  $\rho$  and  $\omega$  mesons couple strongly to the 2 and 3 channels, respectively. The analogy between the  $\rho$  and  $\omega$  masses indicates, however, that vector meson masses are not driven by their meson content, but are rather of QCD origin [15].

## 2.2 Continuum sources

Sources other than vector mesons are known to contribute to the dilepton signal. For instance, Dalitz decays of the  $\Delta$  resonance and of  $\eta$  mesons contribute dominantly at pair masses below about  $0.5 \text{ GeV}/c^2$  [16]. Dilepton production by bremsstrahlung processes has been shown to reveal information on the nucleon electromagnetic form factor in the time-like region around the vector meson masses which is otherwise not accessible [17]. Medium modifications of these continuum sources can be established by comparing heavy-ion dilepton data to model calculations. These model predictions are derived by folding the elementary cross sections and form factors as measured in pion and proton induced reactions into the phase space evolution of heavy-ion collisions [18–20]. Estimates of the total dilepton yield expected in heavy-ion reactions have been carried out within the BUU and the QMD models [16, 21]. Pion and kaon annihilation contributes to the dilepton signal in heavy-ion collisions [22, 23]. This component, greatly suppressed or absent in hadron induced reactions, can be established by measuring the collision system and beam energy systematics of the dilepton signal. Additionally, the decay anisotropy is a powerful tool for unfolding the various dilepton production mechanisms involved [24].

## 3 Design principles

The proposed spectrometer has to be able to cope with very heavy collision systems. At the highest beam energies at SIS, a multiplicity of 200 charged hadrons and of about 30 photons is reached in very heavy collision systems like  $\text{Au} + \text{Au}$ . Thus, a high granularity of all detector systems is necessary in order to minimize the double hit probability in the individual detector modules. The small dilepton branching ratio of the vector mesons, being on the order of  $10^{-5}$ , results in a low yield of the  $e^+e^-$  signal per central heavy-ion event. The system therefore has to have a large geometrical acceptance. Moreover, the system has to be able to operate at the high beam intensities available at SIS. The high interaction rate together with the high hadron multiplicity resulting from the large acceptance represents a serious challenge to the trigger system which has to filter out events containing lepton tracks. The identification of these leptons can only be achieved by detectors which are highly insensitive to the large existing hadron flux. Thus, only hadron blind detectors operating on a fast time scale are capable of meeting the stringent trigger requirements for lepton identification. In order to minimize background due to lepton misidentification at typically prevailing  $e^-/p^+$  ratios of  $10^{-4}$ , redundant recognition of lepton tracks is essential. For the range of momenta considered here ( $0.1 \text{ GeV}/c \leq p \leq 1.0 \text{ GeV}/c$ ), electrons as compared to muons offer the advantage of identification in a hadron blind gas Cherenkov detector

with threshold  $\text{thr} = 20$ . In this paper, the terms dileptons and dielectrons are therefore used synonymously. Last, but not least, is the requirement of accuracy in the measurement of lepton trajectories. The invariant pair mass depends on the single trajectories momentum as well as on their opening angle. The pair mass resolution has to be sufficient to detect changes of the in-medium widths of the  $\rho$  and  $\omega$  mesons. The pair mass resolution should therefore be comparable to the natural width of these states which is about 1%. This requirement subsequently sets conditions on single trajectory momentum resolution as well as on the determination of position which is used for the reconstruction of the pair opening angle.

### 3.1 Basic simulations

In order to determine the basic design parameters of a spectrometer satisfying above criteria, a series of basic simulations was carried out. The phase space distribution of lepton pairs resulting from an uniform mass distribution in the range from  $0.2 \text{ GeV}/c^2$  to  $1.0 \text{ GeV}/c^2$  was studied. The pair energy distribution was assumed to be Maxwellian with inverse slope parameters of 65 MeV and 95 MeV for beam energies of 1 AGeV and 2 AGeV, respectively. This parameterization agrees well with momentum distributions measured in nucleus-nucleus collisions at SIS energies [25]. Figure 1 shows the resulting polar angle correlations for beam energies of 1 AGeV (top) and 2 AGeV (bottom). The shift of the peak towards smaller values at 2 AGeV is due to the larger Lorentz boost at this higher beam energy. The area marked by the dashed lines in figure 1 indicates the range of  $18^\circ$  to  $85^\circ$  chosen as design goal for polar angular acceptance of the spectrometer. The momentum-polar angle correlation resulting from this Boltzmann distribution is shown in figure 2 for beam energies of 1 AGeV (top) and 2 AGeV (bottom). A gain visible is the shift to smaller polar angles at the higher beam energy due to the larger Lorentz boost. At small polar angles, a large range of momenta must be accepted by the spectrometer. The region enclosed by the two dashed lines in figure 2 indicates the polar acceptance as discussed above. Additionally, due to the great interest in the vector meson properties, the dilepton phase space distribution derived from the omega decay was investigated separately. Figure 3 shows the polar angle correlations for the decay of the omega for beam energies of 1 AGeV (top) and 2 AGeV (bottom). The dashed area represents the polar angular acceptance, and contains about 40% of the total intensity. In figure 4, the momentum-momentum correlation of the two leptons from omega decay is shown. If a momentum range of  $0.1 \text{ GeV}/c$  to  $1.5 \text{ GeV}/c$  can be simultaneously analyzed by the spectrometer, then the total omega acceptance is only limited by the polar angular acceptance of 40% mentioned above.

### 3.2 Basic considerations

A lepton pair mass resolution of the spectrometer of 1% is required. This value necessitates a momentum resolution of 1% to 1.5% for lepton tracks with simultaneous acceptance of a momentum range of  $p = 0.1 \text{ GeV}/c$  to  $1.5 \text{ GeV}/c$ . This large momentum range leads to a nonfocusing geometry with a transverse momentum kick  $p_T^F = 0.1 \text{ GeV}/c$ . This value of  $p_T^F$  is equivalent to a value of  $B \cdot l = 0.33 \text{ Tm}$ , where  $l$  represents the path length of the trajectory in the magnetic field of strength  $B$ . If one assumes a value of  $l = 0.5 \text{ m}$  to keep the spectrometer compact, then the magnetic field is less than  $0.7 \text{ T}$ . A transverse momentum kick  $p_T^F = 0.1 \text{ GeV}/c$  puts constraints on the position resolution of the tracking detectors in order to achieve the required momentum resolution. At a momentum of  $1 \text{ GeV}/c$ , the deflection angle equals about  $5.7^\circ$ . A model calculation assuming two sets of two detectors spaced by  $0.3 \text{ m}$  shows that knowledge of position better than  $160 \text{ } \mu\text{m}$  is needed for a relative momentum resolution of 1% at  $1 \text{ GeV}/c$ . In order to account for the multiple scattering contribution to resolution (see below), a position resolution of  $100 \text{ } \mu\text{m}$  is needed. The required momentum resolution can only be achieved by keeping multiple scattering in the magnetic field region small. If only multiple scattering is taken into account, then a momentum resolution of 1% at the minimum momentum acceptance of  $0.1 \text{ GeV}/c$  requires an effective thickness of  $d/L = 0.5\%$ . Here,  $d$  denotes the path length traversed in the material with radiation length  $L$ . This value can only be achieved by filling the space between the detectors with helium.

### 3.3 Basic design

With the considerations outlined above, the basic design requires coverage of the full azimuthal angle and of the polar angular range from  $18^\circ$  to  $85^\circ$  in the forward hemisphere while accepting a momentum range of  $0.1 \text{ GeV}/c$  to  $1.5 \text{ GeV}/c$ . With this design, tracking detectors are needed forward of and behind the magnetic field region for momentum determination. Additionally, two independent lepton identifications should be achieved, one in front of and one behind the magnetic field region. Here, front and back of the field region are defined in the sense of a particle which traverses the magnetic field from the target towards the outer detectors. In the space between target and magnetic field, a ring imaging Cerenkov detector is foreseen. This region therefore has to accommodate a gas radiator. Due to the fixed target kinematics, the hadronic flux is minimal into the backward hemisphere. The hadronic background is therefore minimized if the detector for the Cerenkov photons can be placed in this location. Thus, a mirror arrangement is needed which focuses the Cerenkov photons into the backward hemisphere. In the region behind the magnetic field,

a second, independent lepton identification will be achieved by a combination of time of flight and shower detectors.

### 3.4 Generic acceptance

The generic acceptance resulting from such a design was tested with the pair generator of section 3.1, but extended to invariant pair masses between  $0.01 \text{ GeV}/c^2$  and  $1.5 \text{ GeV}/c^2$ . Figure 5 displays the result obtained for the beam energy of  $1 \text{ AGeV}$ . Shown in this figure is the dilepton acceptance as a function of pair invariant mass and pair transverse momentum. Here, the single lepton acceptance is defined by the polar angular range of  $18^\circ$  to  $85^\circ$  with a low momentum cut at  $0.1 \text{ GeV}/c$ . At high invariant pair masses, the single lepton momenta are above the low momentum cut value. The acceptance is therefore rather flat and reflects the losses due to finite solid angle coverage. At low pair masses, however, the acceptance has a different behavior and depends strongly on pair transverse momentum. The acceptance at high transverse momentum and small masses is significantly increased compared to the high mass value. The two leptons have on average lower momenta when the pair transverse momentum and pair mass are reduced. Therefore, the single trajectory low momentum cut value of  $0.1 \text{ GeV}/c$  is not negligible anymore. This correlation leads to the reduction in acceptance seen in figure 5 for small masses and small transverse momentum values of the pair. The pair acceptance depends on the solid angle covered by the spectrometers as well as on the single lepton low momentum cut imposed by the magnetic field. Operating the spectrometer at a reduced field value results in a reduced single trajectory low momentum cut, albeit at the expense of compromising on resolution. Figure 6 shows the ratio of the two acceptance values, the one obtained with nominal field setting divided by the one with half nominal field setting. Values different than unity in figure 6 reflect directly the amount of pair acceptance lost due to the single lepton momentum cut. The normalized acceptance shown in figure 6 is unity for high pair masses, reflecting the fact that all single particle momenta are larger than  $0.1 \text{ GeV}/c$  in this part of phase space. At low masses, however, the pair acceptance losses due to the single lepton momentum cut can be significant.

## 4 Field configuration

Both toroidal and solenoidal geometries were examined whether they can match the criteria outlined above.

## 4.1 Solenoidal field

In a solenoidal geometry, a field free region around the target needed for the Cerenkov detector can only be approximated by (superconducting) correction coils. At small polar angles, the field direction is nearly parallel to the particle direction resulting in a reduced transverse kick. In this angular range, however, the largest particle momenta have to be measured as can be seen in figure 2.0. Outside the spectrometer, the magnetic field lines occupy a large volume resulting in a high field energy and in the need to shield field sensitive equipment. A massive iron yoke would partially solve these problems, but would constitute a strong background source due to the production of secondary particles[5].

## 4.2 Toroidal field

The toroidal field geometry matches above criteria much better. The shadow of the coils can be aligned with the detector frames such that no additional loss of solid angle is caused by the coils. Although the field strength is rather low, superconducting coils are necessary for a compact coil construction. A normal conducting spectrometer, covering about the same solid angle as a superconducting one with heat shields and vacuum chamber included, would result in a power consumption of about 10 MW. Although such a concept might be technically feasible, the operating costs would exceed the cost reduction for construction within less than two years. These considerations resulted in a field geometry based on a superconducting toroid as the field of choice for the HADES spectrometer.

## 4.3 The Superconducting Toroid

The toroid chosen consists of 6 coils surrounding the beam axis. Each coil is placed in its own vacuum chamber. The six vacuum chambers are connected to a support ring upstream of the target. In this support ring, feed lines for electric power, for liquid nitrogen and for liquid helium connect to the individual coils. At the downstream end, a hexagonal plate holds the six vacuum chambers in place and compensates the magnetic forces acting on the coil cases. Each coil consists of a straight entrance and exit section connected by two arcs. The angles of the entrance and exit sections of  $40^\circ$  and  $45^\circ$  with respect to the beam line were chosen to minimize the azimuthal deflection of particles over the whole polar angular range of  $18^\circ$  to  $85^\circ$ . Due to the V-shape of the coil, a small net focusing with respect to the azimuthal angles is obtained. The shape and orientation of the coil results in a stronger transverse

momentum kick at small polar angles as listed in Table 1. For beam energies of 1-2 AGeV, the transverse momentum kick provided by the field follows approximately the kinematical variation of the particle momenta with polar angle. Figure 7 shows contour plots of the main magnetic field component at azimuthal angles of  $\phi = 0^\circ$  (top) and  $\phi = 25^\circ$  (bottom). The maximum field of 3.7 T is obtained at the coil surface inside the forward arc. In between the coils, i.e., at the azimuthal angle of  $0^\circ$ , the field extends over a wider region as compared to the azimuthal angle of  $25^\circ$  which is close to the coil.

## 5 Spectrometer setup

The HADES spectrometer system is divided into six equal azimuthal sectors of  $60^\circ$  each. Figure 8 shows a schematic view in a midplane of one of these sectors with an outline of the main detector components. For comparison, coils are rotated into the plane shown. A three dimensional view of HADES is shown in figure 9. Two of the azimuthal sectors are removed for better visualization of the interior details of the spectrometer.

### 5.1 Ring Imaging Cerenkov Detector

The Ring Imaging Cerenkov Detector (RICH) has the task of identifying lepton tracks forward of the magnetic field. This system should be able to operate in an hadronic multiplicity environment which can be as high as 200 for central Au+Au collisions. In order to suppress this hadronic background efficiently, a gas radiator with a threshold  $\beta_{thr} = 20$  is chosen. The radiator volume fills the space between the target and the first tracking detector in front of the magnetic field. Since the photon detector must be placed upstream of the target as described in section 3.3, the optical system has to reflect the Cerenkov photons into the backward hemisphere. Thus, the focusing properties of mirrors with different geometrical shapes have been investigated. A spherical mirror is chosen which covers the full azimuthal range and the polar angular range from  $16^\circ$  to  $88^\circ$ . With this geometry, trajectory lengths in the radiator vary from 40 cm at the low polar angles to 70 cm at the large polar angles. The optical properties of the mirror geometry lead to two different focal surfaces in azimuthal and radial direction at large polar angles. The position and orientation of the Cerenkov photon detectors are subsequently chosen such that the two curved focal surfaces are best approximated by the flat cathode plane of the detector [26]. To ensure operation at maximum interaction rate, the photon detector has to have fast response and accurate timing. In order to meet this requirement, a solid state CsI photoconverter is evaporated onto the cathode plane. The position information of the individually registered Cerenkov pho-

tons is contained in the cathode pads carrying the induced signal[27]. All the pad signals are input to the second level trigger for identifying lepton tracks.

## 5.2 Multiplicity/Electron Trigger Array

The Multiplicity/Electron Trigger Array (META) has the task of fast identification of lepton tracks behind the magnetic field. Moreover, this system should be able to deliver a fast event characterization after about 400 ns by measuring charged particle multiplicity. This fast event characterization is needed to select central events at the first trigger level. The detector system chosen for event characterization is an array of time of flight (TOF) paddles. The segmentation of this array is chosen such that the varying width of the paddles results in an approximately constant paddle occupancy in the polar angular range covered. Due to the larger hadron momenta at polar angles  $> 45^\circ$ , time of flight alone is not sufficient in this angular range for the required hadron suppression. At these angles, the TOF array is therefore complemented by an electromagnetic shower detector. This detector consists of a stack of three gas detectors interspaced by two lead converters of two radiation lengths thickness each. The electromagnetic shower signal initiated by a lepton is amplified in the gas detectors and read out through cathode pads[28].

## 5.3 Multiwire Drift Chambers

Multiwire Drift Chambers (MDC) measure the tracks on either side of the magnetic field. Each MDC module consists of a stack of six independent drift cell layers[6]. Two modules in front of and two behind the field allow to measure track pieces which are straight in first order. These track pieces are subsequently used for momentum reconstruction. The position and orientation of the four MDC's are chosen within the available space such that the resulting lever arms in front of and behind the field are maximal. This geometry allows an independent matching of the two measured track pieces to the information of the RICH and META, respectively. The recognition of close trajectories in the first two MDC's forward of the magnetic field allows an improved rejection of track pairs originating from external conversion processes. Additionally, the reconstruction of the deflection angle and, therefore, momentum is not affected by the straggling in target, radiator gas, mirror and detector windows between the point of production and first tracking detector. First tests with prototype drift chambers operated with a He/isobutane gas mixture produced a measured position resolution of 110  $\mu\text{m}$  in a single layer[30]. This value results in a resolution of the whole chamber better than the required value of 100  $\mu\text{m}$  estimated in section 3.2.

## 5.4 Trigger system

A fast, highly selective multi level trigger system combines the information from the RICH, META and MDC's and selects the events of interest. A minimum charged particle multiplicity in each of the six azimuthal sectors defines the first level trigger within a time span of 400 ns after the reaction. For the heavy system Au+Au at a beam energy of 1 AGeV, for example, this requirement results in an event reduction by a factor larger than 10 with an efficiency better than 95% for the most central events [29]. The interaction rate of  $10^6/s$  and the event reduction achieved by the first level trigger define the processing time available for the next trigger stage at 10 ns. This second level trigger requires that leptons be identified in the RICH as well as in the META. Hence, the approximately forty thousand pads of the RICH UV detector have to be searched for rings and the twenty thousand pads of the META detector have to be scanned for showers within 10 ns. This considerable pattern recognition problem is solved by using arrays of FPGA chips (XILINX) [30]. Identified RICH rings and recognized META showers are subsequently input to an angle matching unit. This unit checks whether combinations of ring and shower centers exist which satisfy the polar and azimuthal angle correlations of physical tracks. For a second level trigger, at least two valid combinations have to exist within the event. Moreover, the identified pair has to satisfy additional criteria such as minimum invariant mass or minimum opening angle. For the Au+Au system, for example, the second level trigger results in a further event reduction by a factor of about 100 [6]. The third level trigger combines the output of the angle matching unit with the tracking information from the MDC. This stage mainly rejects combinations of low energy leptons producing a RICH ring with hadrons misidentified as leptons in the META system. In the Au+Au system, the third level trigger results in a further event reduction by a factor of about 10. It is foreseen that HADES operates with different collision systems at beam intensities of  $10^8/s$ . Hence, a 1% interaction target results in  $10^6$  minimum bias events per second. The three stage trigger system outlined above reduces the rate of  $10^6/s$  to a rate of about  $10^2/s$  which will be written onto tape.

## 6 Performance

The performance of the HADES spectrometer was studied by detailed simulations using GEANT [31]. A three dimensional magnetic field map based on the toroidal coil geometry was used for realistic tracking. The whole geometry was implemented and realistic parameterizations of detector resolutions were used [32]. For these simulations, lepton pairs from Maxwell-Boltzmann distributions with inverse slope parameters of 65 MeV and 95 MeV were used for

the beam energies of 1 AGeV and 2 AGeV, respectively.

## 6.1 Acceptance

The geometrical acceptance of the HADES spectrometer was investigated by separating the mass range into three bins. The highest bin represents the mass range of the vector mesons and extends from  $0.5 \text{ GeV}/c^2$  to  $1.2 \text{ GeV}/c^2$ . An intermediate range is defined from  $0.3 \text{ GeV}/c^2$  to  $0.5 \text{ GeV}/c^2$ . A low mass bin covers the range from  $0.1 \text{ GeV}/c^2$  to  $0.3 \text{ GeV}/c^2$ . Here, only the geometrical acceptance including the effect of the magnetic field is investigated. Losses due to detector inefficiencies depend strongly on the particle multiplicity environment, i.e., on the collision system. A study of detector efficiencies will be the subject of forthcoming publications.

### 6.1.1 Transverse momentum acceptance

The transverse momentum acceptance at the beam energy of 1 AGeV is shown in figure 10 for the three mass bins defined above. Shown in this figure are the data points for the acceptance together with second order polynomial fits (solid lines), illustrating the qualitative behavior of the acceptance. For the vector meson mass range, the acceptance has an approximately constant value of 0.4. On the contrary, the low mass range exhibits a significant transverse momentum dependence, as can be seen in the top part of figure 10. The intermediate mass range, displayed in the center of figure 10, also shows a transverse momentum dependence, even though considerably reduced as compared to the low mass range. The transverse momentum acceptance displayed in figure 10 is in qualitative agreement with the discussion of generic acceptance in section 3.4.

### 6.1.2 Rapidity acceptance

The rapidity acceptance at a beam energy of 1 AGeV is shown in figure 11. Shown in this figure are the primary distribution (dotted line histogram) and the accepted distribution (solid line histogram). These two distributions are shown in arbitrary units and refer to the vertical scale on the left of figure 11. The acceptance is defined by the ratio of these two distributions and refers to the vertical scale on the right. The acceptance is shown by the data points (triangles) together with a second order polynomial fit (dashed line). The top and bottom part of figure 11 show the rapidity acceptance for the low and high mass range, respectively.

### 6.1.3 Mass acceptance

The acceptance as a function of invariant pair mass is shown in figure 12. The solid line represents a second order polynomial fit. The mass dependence of the acceptance results from folding the Boltzmann pair transverse momentum distribution with the transverse momentum acceptance displayed in figure 10. Thus, the mass dependence of the acceptance shown in figure 12 is in first order defined by the transverse momentum acceptance (shown in figure 10) at the average pair transverse momentum.

## 6.2 Resolution

### 6.2.1 Single track momentum resolution

The momentum resolution of the spectrometer is determined by multiple scattering as well as by the position resolution of the MDC's. The MDC modules are designed such that the position resolution in polar direction is about a factor of two better than in the perpendicular direction. Here, polar direction denotes the direction defined by varying the polar angle at a fixed azimuth. The y-axis is taken to be in polar direction whereas the x-axis is the perpendicular direction within the MDC wire planes. The better position resolution in y-direction results in an improved momentum resolution since the main deflection occurs in this direction. The better y-resolution is obtained by the wire orientation in a MDC module at angles of  $0^\circ$ ,  $20^\circ$  and  $40^\circ$  relative to the x-direction. The single track momentum resolution is investigated by using a thermal source with masses uniform between  $0.1 \text{ GeV}/c^2$  and  $1.2 \text{ GeV}/c^2$  decaying into  $e^+e^-$  pairs. The reconstruction of the trajectory is carried out by an algorithm which fits the ve kinematical parameters simultaneously and which does not make assumptions on knowledge of the vertex. Numerical values for resolution given below are in units of standard deviation unless explicitly stated otherwise. Figure 13 shows the momentum resolution for various position resolutions of the MDC's for electrons (top) and positrons (bottom). The curve labeled "no multiple scattering" is derived by switching off the multiple scattering mechanism in the GEANT simulations, and by assuming infinitely good position resolution  $x = y = 0$ . This curve contains the effects of energy loss straggling of the lepton tracks as well as the finite accuracy inherent in the fit procedure used for reconstructing the momenta. The effects of multiple scattering are investigated by analyzing tracks with the multiple scattering switch on. The finite position resolution is taken into account by adding a Gaussian distributed uncertainty to the position values obtained in the simulations. The position resolutions  $x$  and  $y$  specified in figure 13 are the resolutions for one complete MDC, i.e., the value derived when using the information of all six wire planes of one MDC module. The values

shown in figure 13 represent the full angular range accepted by the spectrometer. The finite position resolutions of the MDC's become more important at large momenta as is visible in figure 13. The anticipated time resolution of the drift cells results in position resolutions of the whole MDC set of  $y = 80 \mu\text{m}$  and  $x = 160 \mu\text{m}$ . Thus, a momentum resolution of about 1% at a momentum of  $1 \text{ GeV}/c$  is expected. The momentum resolution for different polar angles is shown in figure 14. The solid line displays the relative momentum resolution for polar angles  $60^\circ$ . The dotted and dashed curves in figure 14 represent the resolution for polar angles  $40^\circ$  and for  $40^\circ$  to  $60^\circ$ , respectively. Even though the transverse momentum kick due to the magnetic field decreases towards larger polar angles by a factor of two, the momentum resolution degrades only by about 20%. Due to the kinematical variation of mean momentum with polar angle as shown in figure 2, the average momentum resolution is approximately constant over the whole angular range.

## 6.2.2 Pair mass resolution

The absolute and relative pair mass resolution as a function of pair mass are shown in the top and bottom part of figure 15, respectively. The mass resolution is shown for single track position resolutions of 0, 60, 80 and 100  $\mu\text{m}$  in y-direction. The anticipated MDC resolution of  $y = 80 \mu\text{m}$  is indicated by the solid line. At masses larger than  $0.7 \text{ GeV}/c^2$  approximately, the mass resolution is dominated by the contribution of position resolution. Below masses of  $0.4 \text{ GeV}/c^2$ , the absolute resolution is almost constant, irrespective of position resolution. From the dependence of the invariant mass on momenta and relative angle of the two leptons and from the momentum resolutions shown in figure 13, the inaccuracy of the pair opening angle can be determined as source of this behavior. This inaccuracy is due to multiple scattering in the target, the RICH radiator and the mirror. A refined software algorithm which includes the angle information of the RICH might improve the resolution for low masses. From these simulations, a relative mass resolution of  $M/M = 0.8\%$  ( ) can be expected in the mass region above  $0.4 \text{ GeV}/c^2$ . This value is slightly better than the original design value of 1% outlined in section 3.2.

## 7 Conclusions

HADES is a new generation spectrometer designed to measure electron pairs emitted in nucleus-nucleus collisions at beam energies of 1-2 A GeV and in hadron induced reactions. The setup is optimized for maximum geometrical acceptance. Background due to misidentified hadrons is kept low due to redundant lepton identification. Particular emphasis is placed on good mass resolution in order to measure medium properties of the vector mesons  $\rho, \omega, \phi$ !

and . The resulting performance shows a geometrical acceptance of about 40% and an excellent mass resolution of 1% for lepton pairs from  $\Delta$  decays. Radiative decays of  $\Delta$  and  $N^*$  resonances can be studied in order to investigate the resonance matter produced at SIS energies.

#### Acknowledgements

The HADES collaboration is grateful to GyWOLF and LWINCKEMANN for their advice concerning BUU and QMD calculations. Fruitful discussions with members of the DLS and of the CERES collaboration are gratefully acknowledged. The HADES project is supported in part by the following contracts: EC within the TMR program contracts ERBCHRX-CT 94-0634 and ERBCIPD-CT 94-0091, INTAS foundation Brussels contract 94-1233, DAAD contract 312/programm-bokeneyer, Stiftung Deutsch-Polnische Zusammenarbeit JUMBO, Warsaw contract 528/92/LN, German BMBF contracts G I 475 TP 4, O F 474 TP 4, T M 353 TP 6, the GSI-Hochschulprogramm, and the French-German collaboration agreement IN 2P 3-D SM /CEA and GSI.

## References

- [1] A Yegneswaran et al, Nucl. Inst and Meth. A 290, (1990) 61
- [2] W K Wilson et al, Phys. Lett. B 316, (1993) 245;  
H Z Huang et al, Phys. Rev. C 49, (1994) 314
- [3] R Baur et al, Nucl. Inst. and Meth. A 343, (1994) 87
- [4] G Agakichiev et al, PRL 75, (1995) 1272
- [5] The HADES collaboration, Letter of Intent for a High Acceptance Dielectron Spectrometer, GSI 1993
- [6] The HADES collaboration, Proposal for a High Acceptance Dielectron Spectrometer, GSI 1994
- [7] V Metz, Newsletter 11, Vol2, (1995) 159
- [8] G E Brown and M Rho, Phys Rev Lett. 66, (1991) 2720;  
G E Brown and M Rho, Nucl Phys. A 596, (1996) 503
- [9] M Lutz, S Klimt and W Weise, Nucl Phys. A 542, (1992) 521
- [10] T Hatsuda and S H Lee, Phys Rev. C 46, (1992) R 34
- [11] M Asakawa and C M Ko, Nucl Phys. A 560, (1993) 399;  
M Asakawa and C M Ko, Nucl Phys. A 572, (1994) 732
- [12] M Lutz, A Steiner and W Weise, Phys Lett B 278, (1992) 29
- [13] G Chanfray and P Schuck, Nucl Phys. A 545, (1992) 271
- [14] M Hermann, B Friman and W Norenberg, Nucl Phys. A 560, (1993) 411;  
B Friman, preprint GSI-95-24
- [15] M Soyeur, Erice Lectures Notes 1993
- [16] G Wolf, W Cassing and U Mosel, Nucl Phys. A 552, (1993) 549
- [17] H C Donges, M Schafer and U Mosel, Phys Rev C 51, (1995) 950
- [18] H Stoecker and W Greiner, Phys Rep. 137, (1986) 278
- [19] W Cassing, V Metz, U Mosel and K Niita, Phys Rep. 188, (1990) 363
- [20] J Aichelin, Phys Rep. 202, (1991) 233
- [21] L Winkelmann et al, NATO Advanced Studies, Bodrum 1993
- [22] C Gale and J Kapusta, Phys Rev. C 35, (1987) 2107
- [23] H Fujii and T Tatsumi, Prog. Theor. Phys. Suppl. 120, (1995) 289

- [24] E. Bratkovskaya, W. Cassing and U. Mosel, submitted to Phys.Lett.B;  
E. Bratkovskaya, O. Teryaev and V. Toneev, Phys.Lett. B 348, (1995) 283
- [25] V. Metzger, Prog.Part.NuclPhys. 30, (1993) 75
- [26] H. Schon, PhD thesis, University of Frankfurt, 1996
- [27] R. Gemhauser et al., submitted to Nucl. Instr. and Meth.
- [28] P. Salabura et al., Acta Physica Polonica B 27, 1-2, (1996) 421
- [29] R. Schicker et al., Univ. Cyprus preprint UCY-PHY-96/04
- [30] The HADES collaboration, Progress Report, GSI Scientific Report 1995
- [31] GEANT 3.21, CERN program library W 5013, CERN Geneva
- [32] W. Karig, diploma thesis, University of Frankfurt, 1993

## Figure Captions

Fig. 1. Polar angle correlation of  $e^+e^-$  pairs emitted from uniform mass distribution for beam energies of 1 AGeV (top) and 2 AGeV (bottom). Contour lines are in steps of 10% of peak intensity. The dashed lines indicate the HADES acceptance.

Fig. 2. Correlation of momentum and polar angle of leptons at beam energies 1 AGeV (top) and 2 AGeV (bottom). Contour lines are in steps of 10% of peak intensity. The dashed lines indicate the HADES acceptance.

Fig. 3. Polar angle correlation of leptons from omega decay at 1 AGeV (top) and 2 AGeV (bottom). Contour lines are in steps of 10% of peak intensity. The dashed lines indicate the HADES acceptance.

Fig. 4. Momentum correlation of leptons from omega decay at 1 AGeV (top) and 2 AGeV (bottom). Contour lines are in steps of 20% of peak intensity.

Fig. 5. Generic pair acceptance as a function of invariant mass and transverse momentum with single trajectory low momentum cut at 0.1 GeV/c.

Fig. 6. Generic pair acceptance with single trajectory low momentum cut at 0.1 GeV/c normalized to acceptance with cut at 0.05 GeV/c.

Fig. 7. Contour plots of the main magnetic field component  $B_z$  in between two coils at  $\theta = 0^\circ$  (top) and  $\theta = 25^\circ$  (bottom) in units of Tesla.

Fig. 8. Schematic view of the HADES setup (see text). The two trajectories show non-originate from the target.

Fig. 9. Three dimensional artistic view of the HADES setup (see text). Two azimuthal segments are removed for better viewing of interior details.

Fig. 10. HADES pair acceptance as a function of pair transverse momentum for low (top), medium (center) and high (bottom) pair masses. The solid lines are second order polynomial fits.

Fig. 11. Rapidity distribution of original (dotted line histogram) and accepted (solid line histogram) lepton pairs (left scale). The triangles represent the rapidity acceptance (right scale).

Fig. 12. Pair acceptance as a function of pair mass. The solid line is a fit to the data points.

Fig. 13. Relative momentum resolution as a function of momentum for electrons (top) and positrons (bottom). The solid line is the expected resolution for HADES.

Fig. 14. Relative momentum resolution as a function of momentum for different polar angle bins for electrons (top) and positrons (bottom).

Fig. 15. Absolute (top) and relative (bottom) invariant mass resolution as a function of invariant mass for different position resolutions of MDC's.

## Tables

[degr]	p [MeV/c]
25	103
45	70
60	62
80	55

Table 1

Transverse momentum kick  $p$  for different polar angles at an azimuthal angle of  $= 15^\circ$  when the field is set at maximum value.

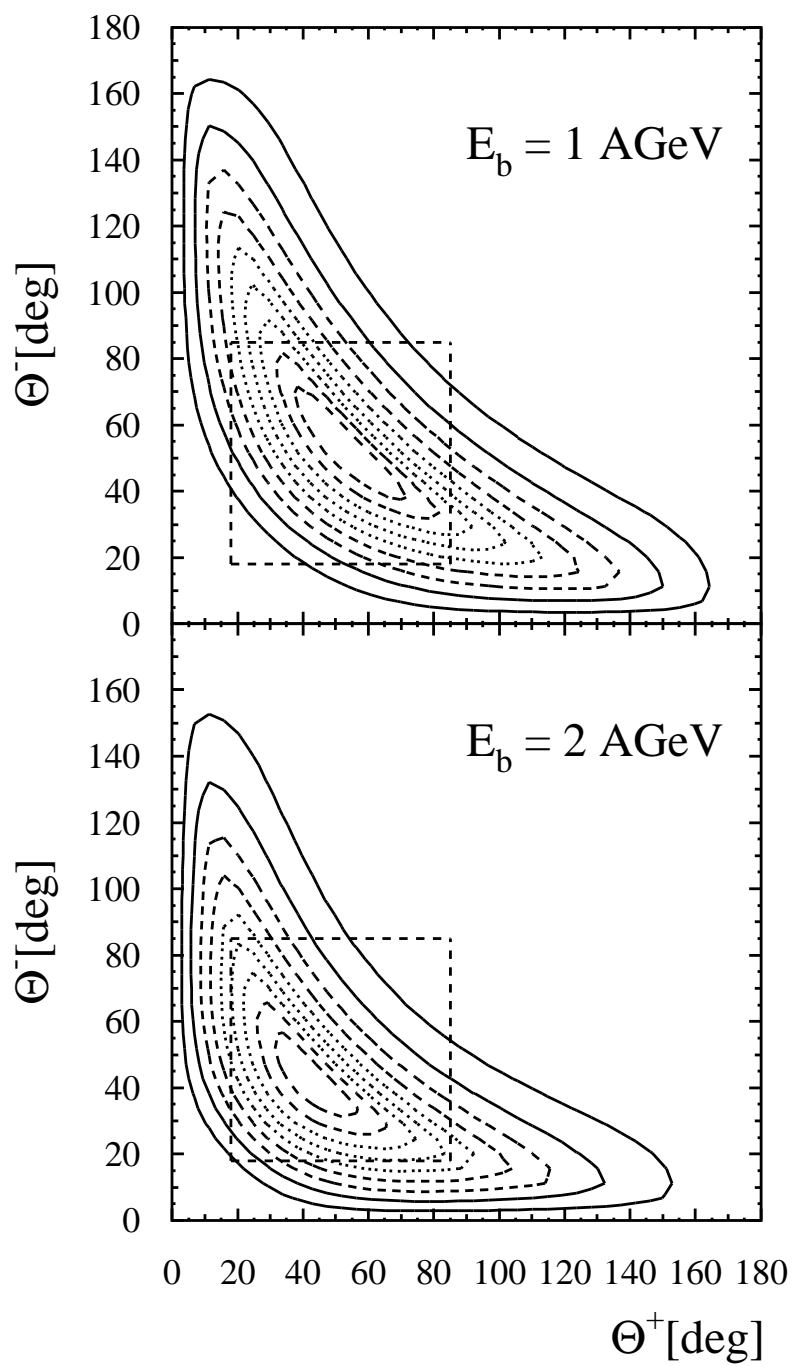


FIG . 1

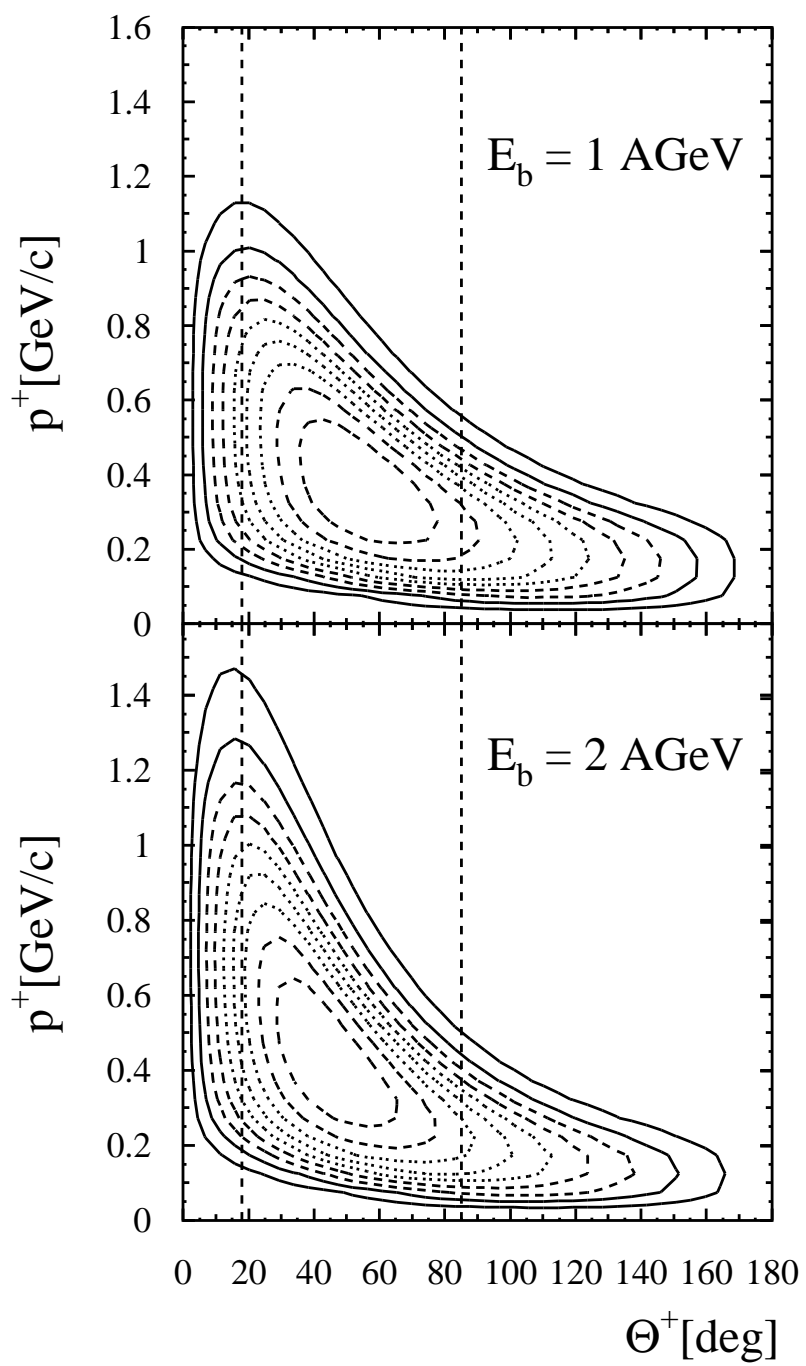


FIG . 2

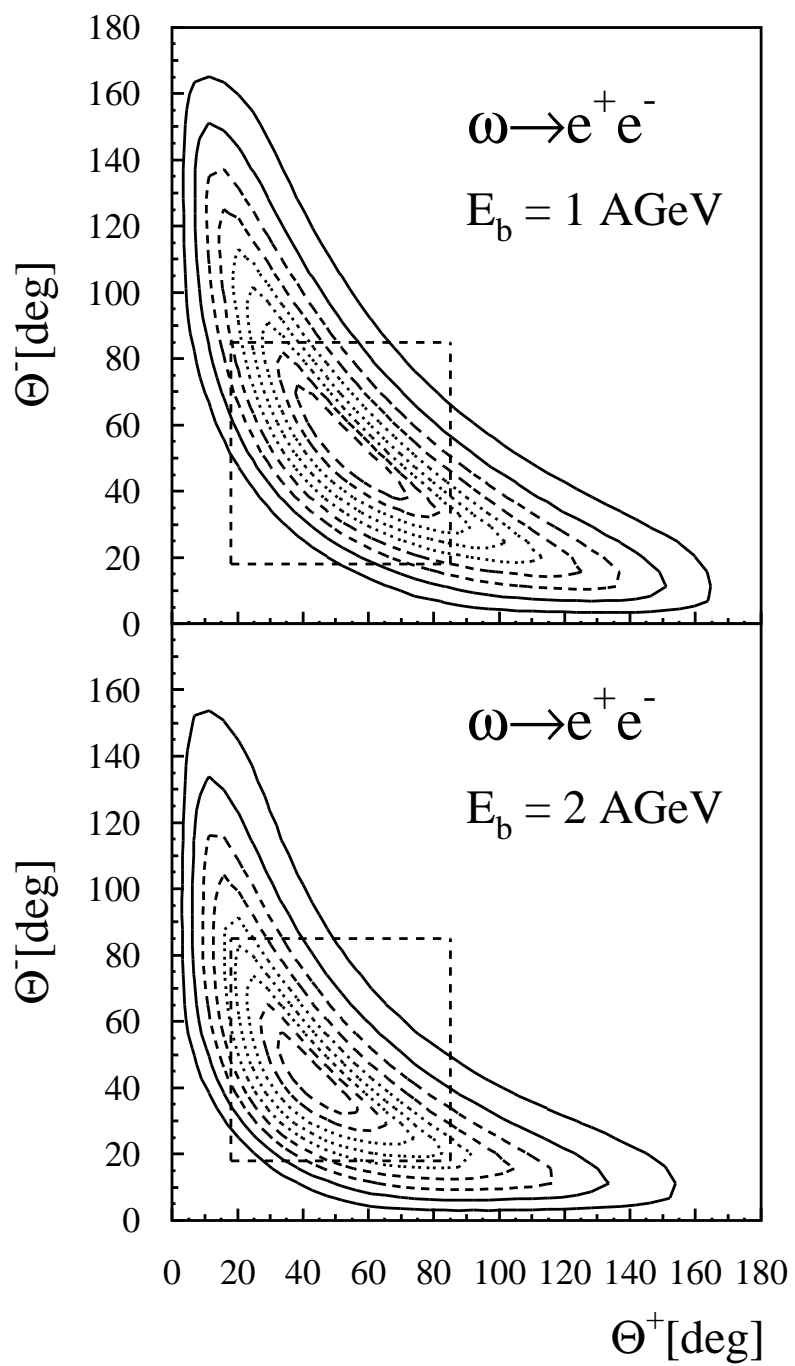


FIG . 3

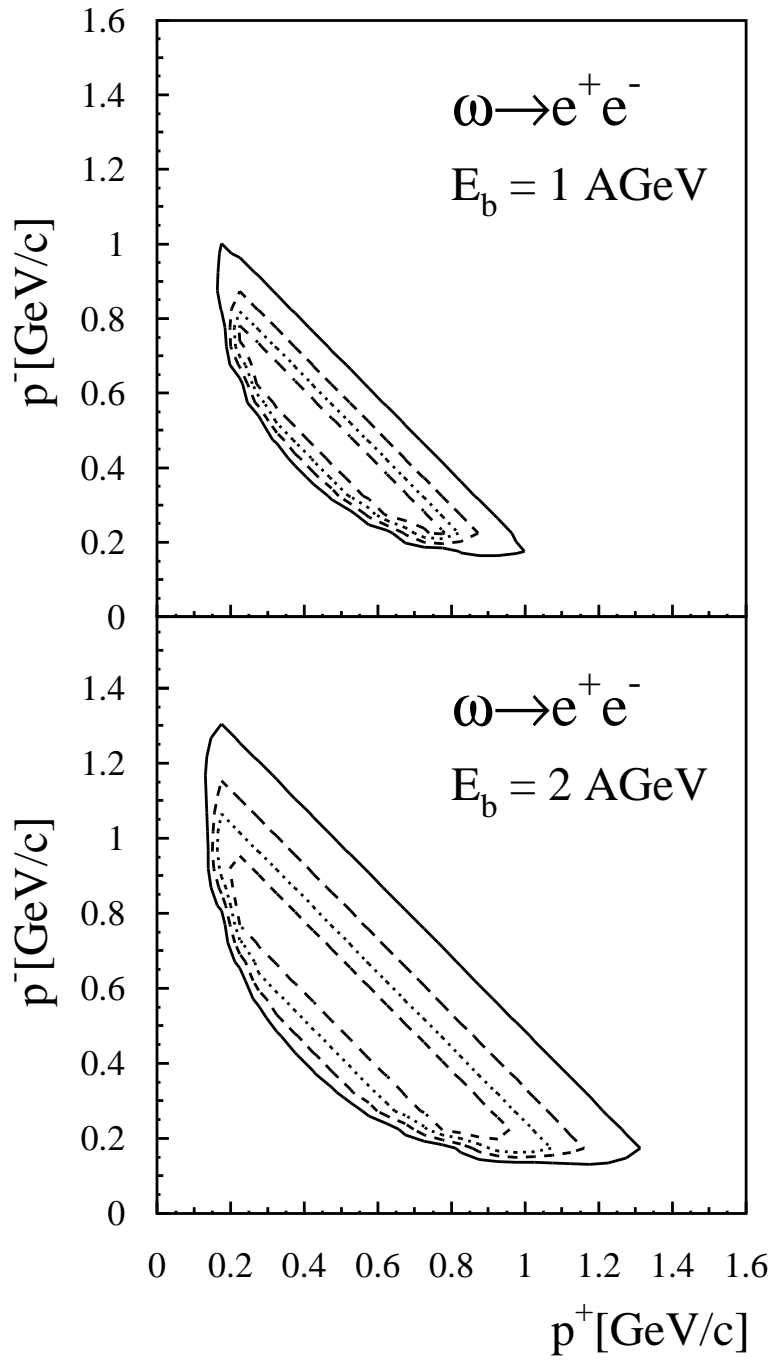


FIG . 4

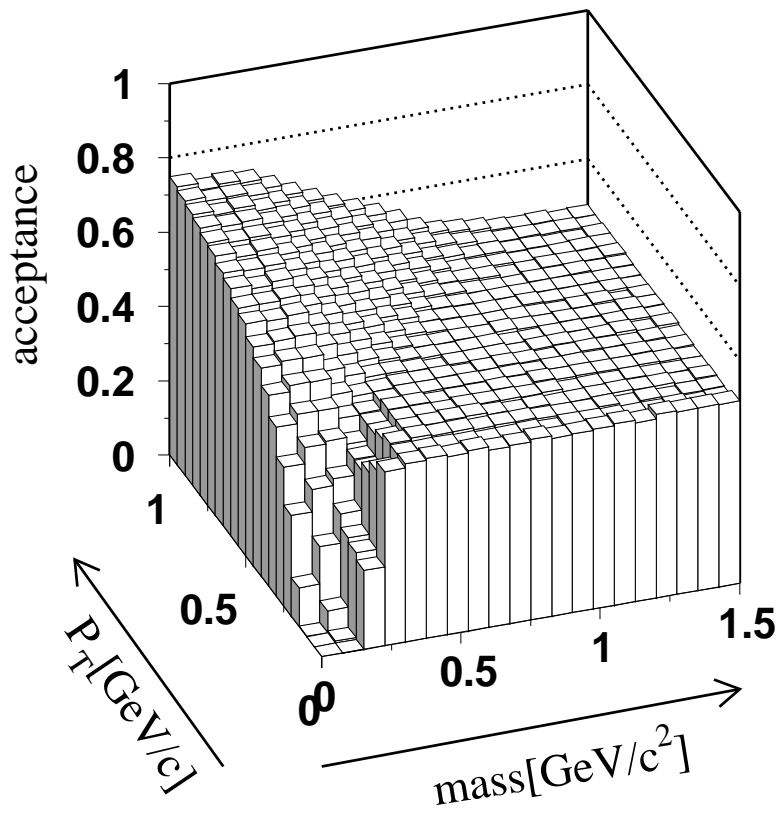


FIG . 5

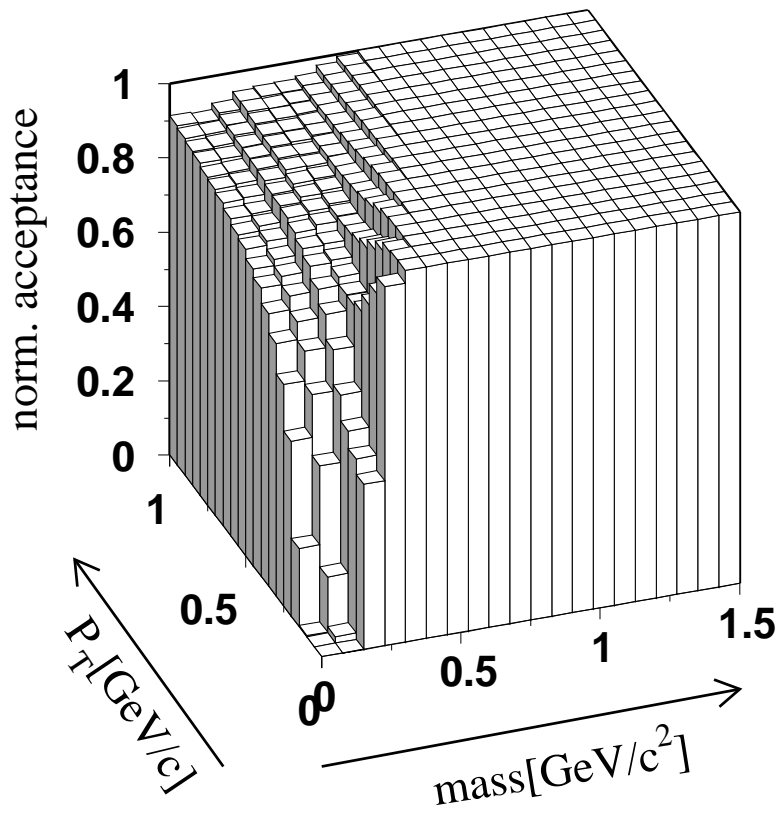


FIG . 6

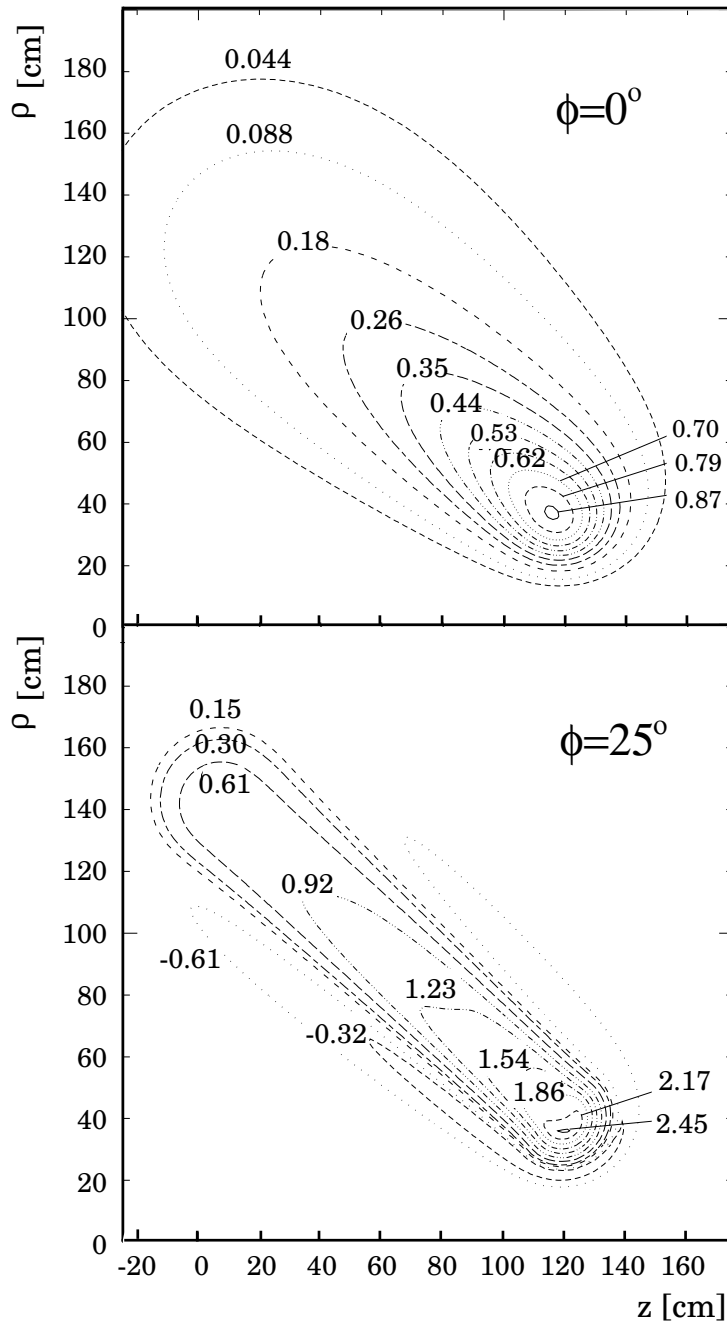


FIG . 7

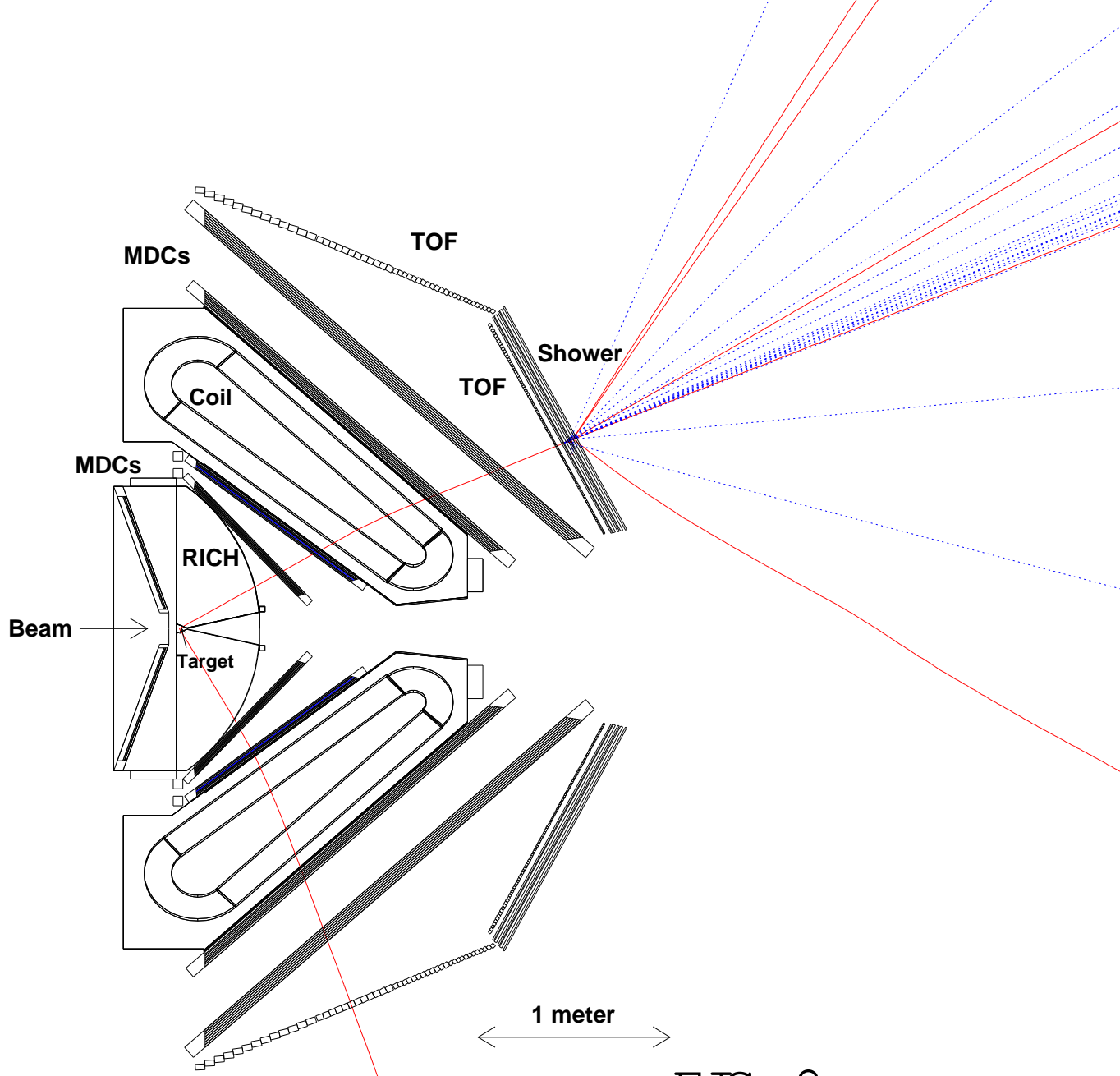


FIG . 8

This figure corresponds to a huge PS-file which can be provided separately upon request from :

"schicker@alpha2.nslucy.ac.cy"

FIG . 9

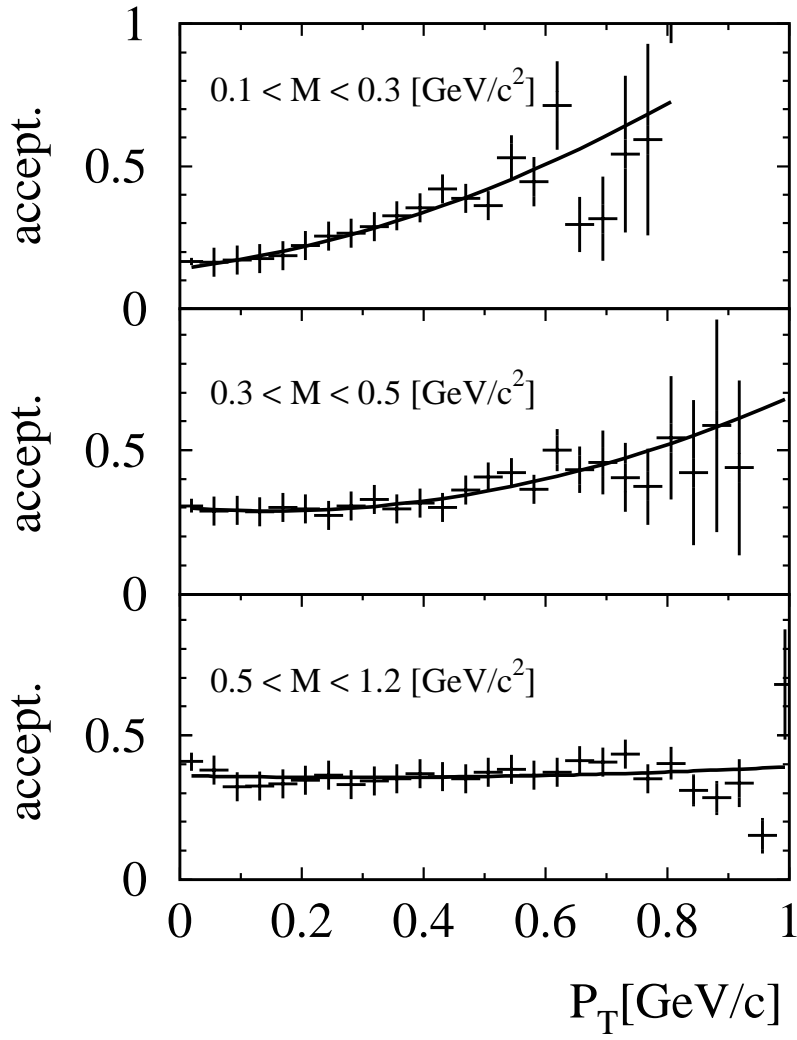


FIG . 10

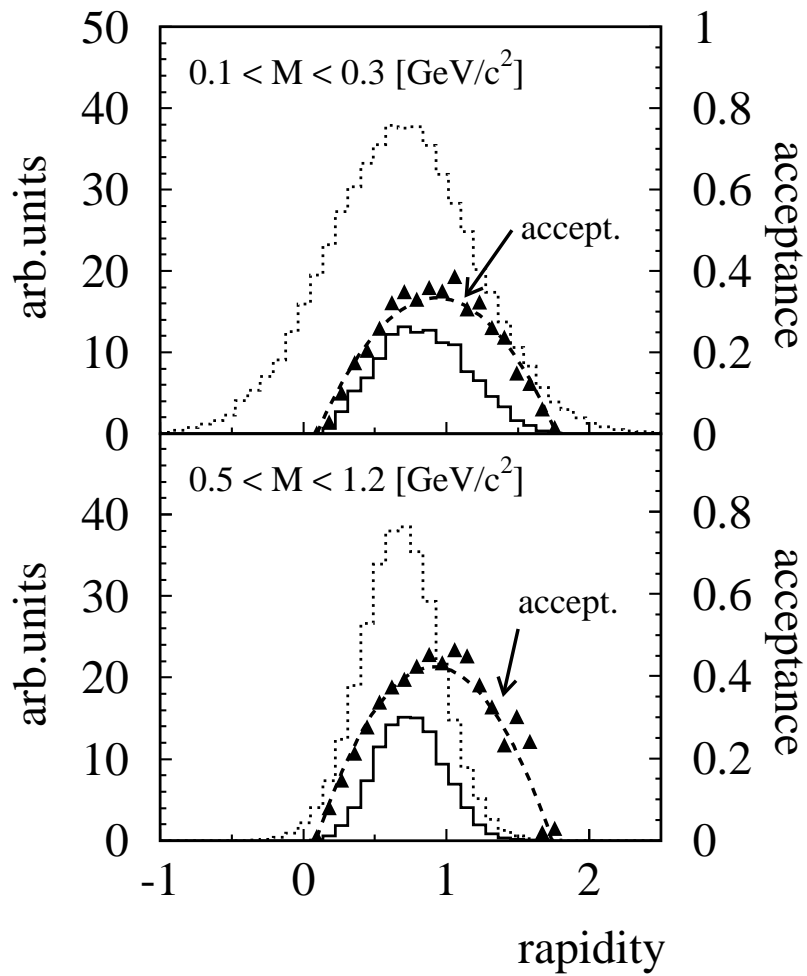


FIG . 11

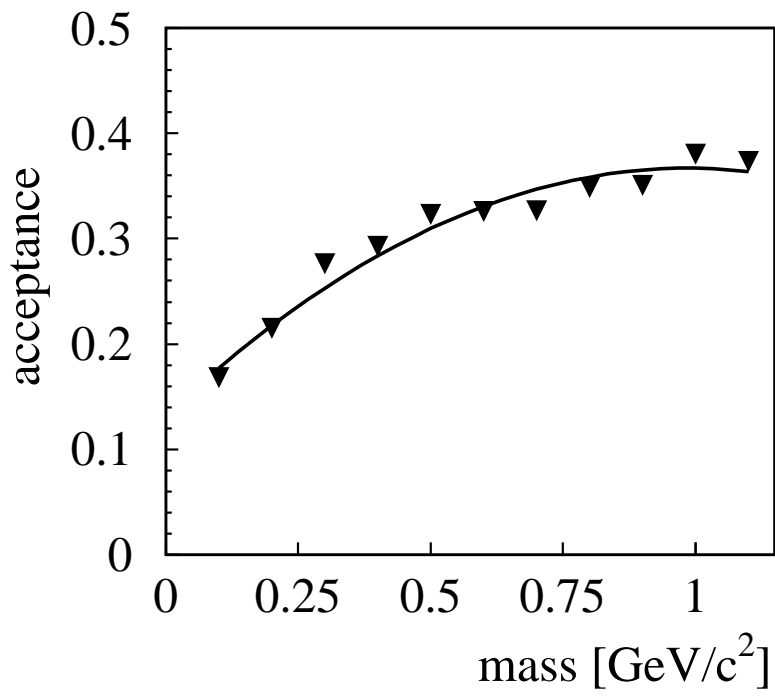


FIG . 12

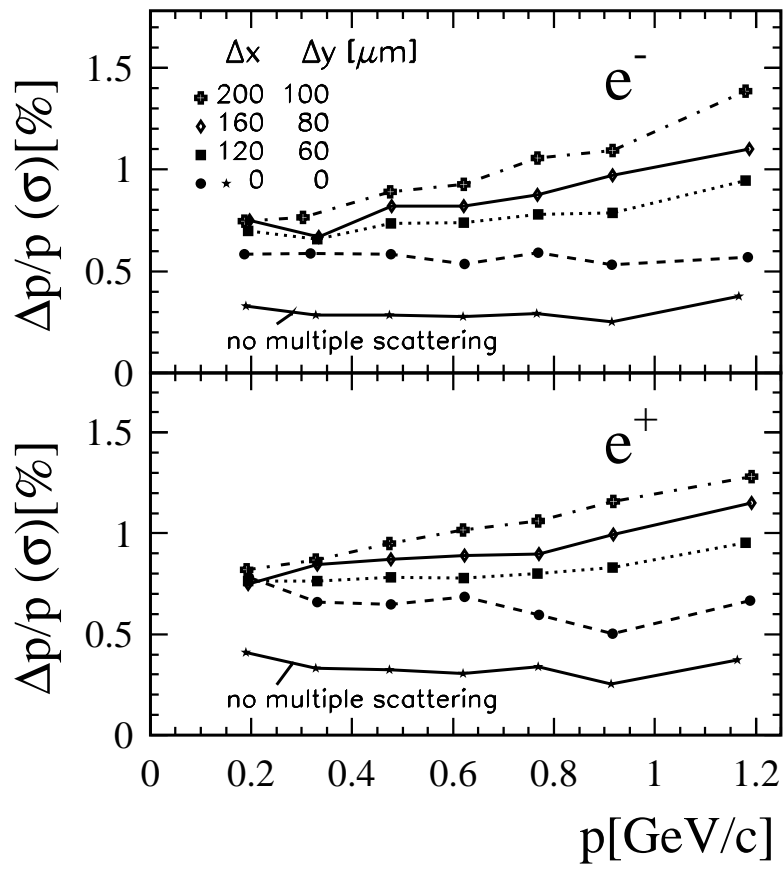


FIG . 13

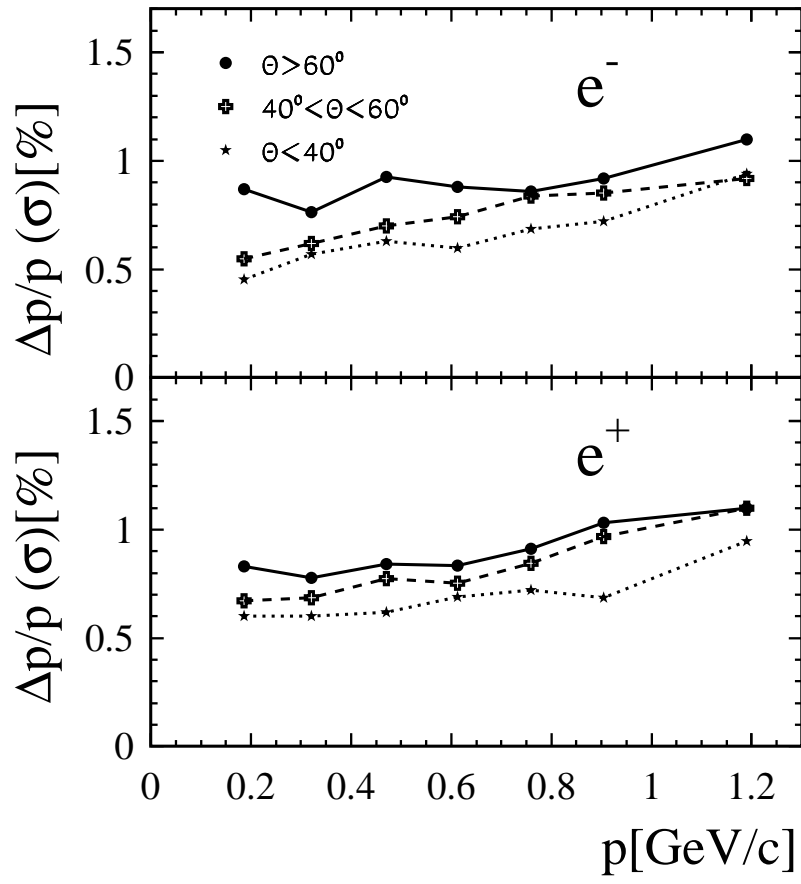


FIG .14

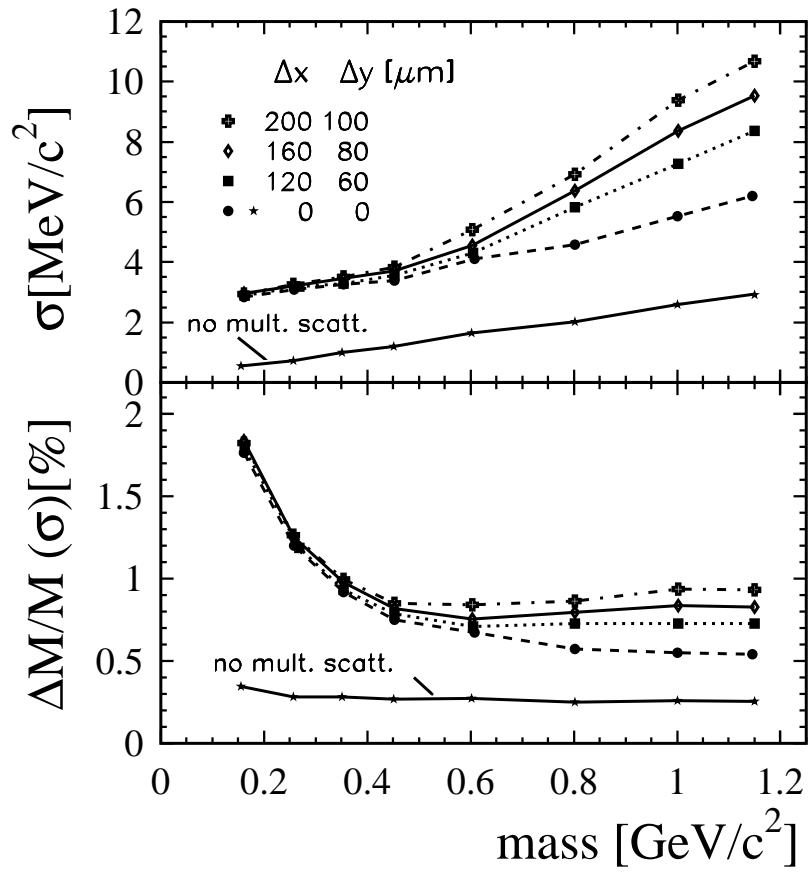


FIG . 15